

## A Promising Comprehensive Optical System Design and Fabrication for Solid-Fuel Characterization of the Missiles Engines

Abdalrhman Adel Mohamed<sup>1</sup>, Osama A. Omer<sup>1</sup>, M. Anwar<sup>2</sup>, Mohamed Alamir<sup>2</sup>  
Amir Almslmany<sup>3</sup>

<sup>1</sup>Comm faculty of engineering, Aswan, <sup>1</sup>Dept. of Electronics & Comm

Faculty of engineering, Aswan, <sup>2</sup> Faculty of Science Aswan University Aswan, Egypt,

<sup>2</sup>Dept. Comm. Alexandria Higher Institute of Engineering and Technology Alexandria, Egypt,

<sup>3</sup>Dept. of Electronics & Comm. Air Defence College, Alexandria University.

**Abstract**— In this paper, present a unique model of a comprehensive spectrograph Systems. the proposed optical system evaluates the performance of solid fuel columns SFC on the basis of spectroscopy, when they are fully combusted and exit the exhaust nozzle of a solid rocket fuel engine SRFE. By collecting and spectroscopic analysis of the radiation emitted by waste chemical compounds in the infrared, visible and ultraviolet ranges. The proposed spectroscopy system design features several optical systems specifically designed for performing spectroscopic measurements remotely. To take into account security and safety. The proposed optical system addresses many of the defects of the traditional systems used in this field. Such as not need to take a sample in a gas cell, like the case in the FTIR technique, and not to be affected by the surrounding environment from radioactive sources, like the case in the spectroscopy technique using visible and ultraviolet light radiation. There is a distinctive optical system for the thermal camera to prevent radiation sources resulting from existing reflections in the test environment, the synchronization time in fast cameras is 15 microseconds, which makes the 3D image formation algorithms work to create an ideal image, thus overcoming the defects of the digital inline holography system.

**Keywords:**— *solid fuel columns (SFC), solid rocket fuel engine (SRFE), Fourier transform infrared spectroscopy(FTIR).*

### 1. Introduction

Rocket engines create hot gases in the combustion chamber, which are then released out the nozzle [1], where they interact with the surrounding air. An afterburning reaction happens at the mixing layer when oxygen particles are pulled into the plume. As a result, both the temperature and the radiation intensity for the gaseous by-products of combustion. As a result, rocket exhaust has tremendous temperatures, velocities, and pressures. strong irradiation. As a result, the temperature of the plume is a crucial indicator of It is the functionality of rocket engines that enables comprehension of internal combustion circumstances. in addition to the overall efficiency of the engine. In the last few decades, solid fuel combustion propulsion has Rocket propulsion technologies for spacecraft have grown more common as a This will help simplify manufacturing and increase security while reducing costs [2].

Solid aluminum fuel and ammonium perchlorate, as well as hydrocarbons and hydroxyl-terminated polybutadiene, are common oxidizers used in solid rocket motors (SRMs) (HTPB). Multiple chemicals, including carbon monoxide (CO), nitrogen (N<sub>2</sub>), hydrogen (H<sub>2</sub>), water (H<sub>2</sub>O), carbon dioxide (CO<sub>2</sub>), and various solid particles, may be found in the SRM exhaust plume. Solid propellants often have additions like boron and aluminum that boost rocket thrust. Some combustion products, such carbon dioxide (CO<sub>2</sub>) and water (H<sub>2</sub>O), as well as solid particles that emit in a continuous spectrum, are the primary contributors of infrared radiation [3].

There are primary spectral bands for CO<sub>2</sub> (2.6–2.8 μm, 4.1–4.5 μm, and 12.5–17.0 μm), and the same is true for water (2.5–2.8 μm, 5.6–7.6 μm, and 12.0–17.0 μm). Two spectral bands, at 4.3 and 2.8 μm, have been shown to be

particularly prominent in previous investigations of rocket plume radiation [4].

optical systems for measuring and calibrating missile systems fuel relies on three carefully designed basic components, which are the multi-wavelength transmitter system to measure the interaction of the laser with the exhaust materials coming out of the fuel when burning at the wavelengths 532 nm to 1064 nm. The second is the receiver works in the range of visible and infrared rays. It receives the rays resulting from the exhaust and its spectral analysis. The third component is the throttle nozzle chamber in which the solid fuel column burns [5].

There are three main spectroscopic analyzes in the measurements of solid fuel rocket exhaust Infrared Spectroscopy Using the Fourier Transform, UV-VIS-IR Spectroscopy and Alumina Emission Measurement (AEM) [6].

The exhaust plume may be studied under a variety of rocket operating parameters using spectroscopy methods, yielding reliable data [7]. The spectroscopic approach stands out because it allows for in-depth research into the emission or absorption spectra of the rocket plume without disrupting the plume's or the environment's physical characteristics [8].

The analysis's goal is to learn about the rocket engine through the study of the radiation spectrum of its exhaust [9]. For the sake of simplification, let's say that photons are the energy-carrying particles that make up electromagnetic waves. With spectroscopy, may use the fact that an object's energy level rises after being hit by a stream of photons [10]. If a sample absorbs a photon. The main contribution of this research The proposed optical system works under the different field atmosphere to test solid rocket fuel engines This paper is organized as follows. Section 2 previous work of optical diagnostic solid propellant fuel, Sec 3 optical proposed system design, Sec 4 results, Sec 5 conclusion [11].

## 2. Previous work of The Optical Diagnostic Solid Propellant

### Fuel:

Spectroscopic techniques rely on the detection of emission, as atoms in the sample will release a photon when they are stimulated by the electromagnetic waves travelling through them. Detecting photon emission is one technique utilized in spectroscopy. UV-VIS spectroscopy and IR spectroscopy, in particular FTIR (Fourier transform infrared) spectroscopy, are two of the most common methods employed in the investigation of rocket engine exhaust gases [12].

### 2.1 FTIR Technique:

Among the many benefits of Fourier transform infrared (FTIR) spectroscopy is the ability to get spectral measurements in real time by collecting data across a large wavelength range with an interferometer [13]. Figure 1 shows the diagram of the FTIR system.

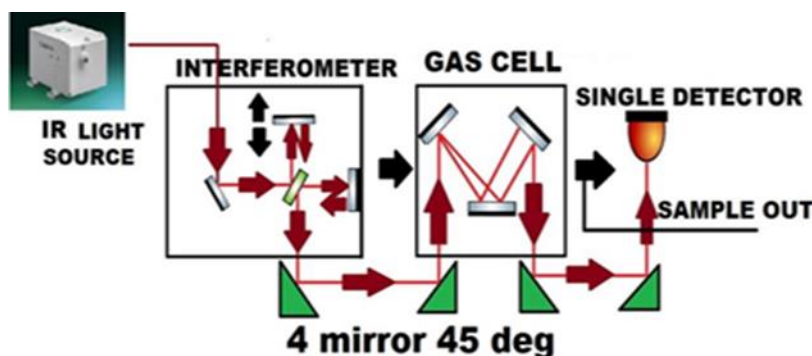


Fig.1. diagram of the FTIR system.

The device consists of an optical beam splitter and two mirrors perpendicular to each other, the first fixed and the second moving [14]. towards the front and back, so that about half of the radiation coming from the source is reflected towards the fixed mirror and is reflected back towards. splitter beam so about half of it a quarter of the original beam passes towards the detector, and when the two mirrors are farther away from the same distance from the splitter beam [15], so the two beams overlap constructively, but when the mirror moves by a quarter of a wave then the overlap the two beams are destructive, and when a monochromatic light is used [16], the detector records a beam whose intensity changes as the mirror moves and when the mirror is moving. Using multi-wavelength light, the detector records the sum of all the waves and when the two mirrors are at the same distance from the splitter

beam [17].

all the waves interfere constructively and we get intense central peaks that record with high clarity. W. Gill et al. at Sandia National Laboratories to monitor plume temperatures of a rocket solid motor operating outside of its design envelope [18]. This research defines the ambient conditions around the plume and analyses its thermochemical and physical characteristics [19].

The experiment was conducted with the propellant consumed under design conditions, that is, at atmospheric pressure, with metal droplets in the hot exhaust gases. Spectroscopy may be used to determine the temperatures of the exhaust plume's various components. in Figure.2. show details of gas cell in FTIR, Where the exhaust of solid fuel combustion is entered, the resulting spectra are extracted from the products of combustion as shown in the figure, then the exhaust gases exit to the outside of the gas cell.

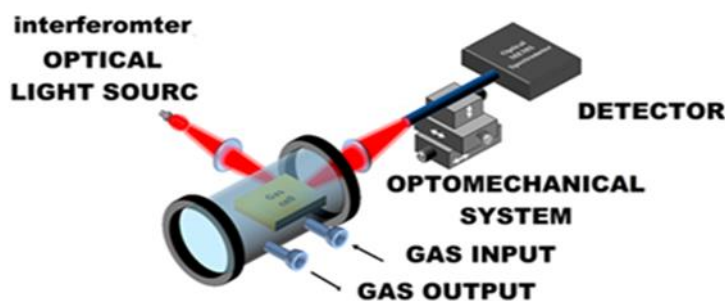


Fig.2. the gas cell of FTIR system.

One of the prominent defects in this technology is that when there is a distortion of the exhaust, non-homogeneous combustion, this system gives completely inaccurate values for the infrared radiation emitted by the exhaust, especially in the case of off axis remotely. Because it depends mainly on taking a sample inside the gas cell. This is not available in the case of taking a small sample of solid fuel inside a chamber and conducting a combustion test on it and entering the combustion product inside the gas cell [20].

### 2.2 Ultraviolet and visible light spectroscopy:

The basic components of UV-visible spectroscopy are identical to those used in infrared spectroscopy [21], with the exception of the interferometer, which is replaced by a monochromator in the UV-visible region. Monochromator is an optical device that sends monochromatic bands of light from a light source to the sample [22]. Monochromator can either be based on filters, which selectively let through a narrow wavelength range, or on a dispersing element, which breaks up the radiation into its component waves so that a specific band can be chosen. in Figure.3. show the optical Spectrometer subsystem.

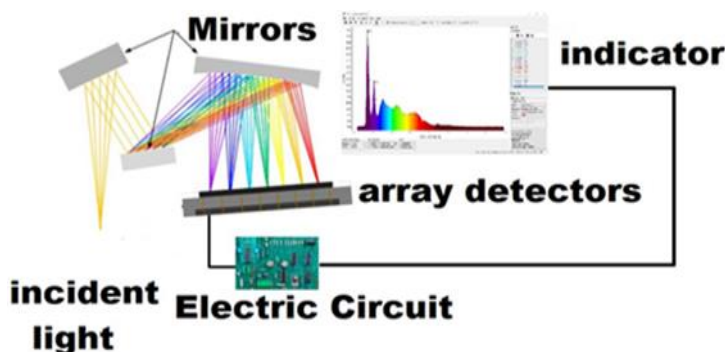


Fig.3. schematic diagram of optical spectrometer

where a number of two devices are used at a certain angle of the solid fuel column in order to perform a visual analysis of the radiation resulting from the products of combustion[23]. in Figure.4. show Two spectrophotometers placed at a certain angle around the solid propellant fuel. in this technique, the solid fuel is placed in the middle of a space between two optical systems with two lights connected to spectrophotometers to measure emissions, from the

combustion exhausts of solid fuels [24], and the information of those spectra is collected by the signal processing system and then entered into the computer to measure the efficiency of combustion.

In this technique, the solid fuel is placed in the middle of a space between two optical systems with two lights connected to spectrophotometers to measure emissions, from the combustion exhausts of solid fuels, and the information of those spectra is collected by the signal processing system and then entered into the computer to measure the efficiency of combustion. The main drawback of this technique is the time it takes before the spectroscopic scan. In addition to any noise caused by light or electronic emitting sources, categorically affect the results of spectroscopy.

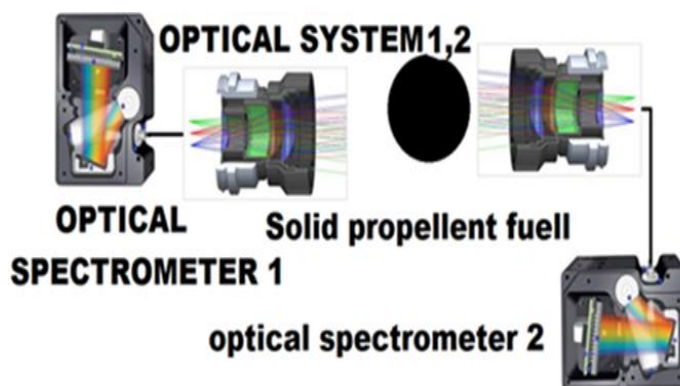


Fig.4. schematic diagram UV and VIS technique

### 2.3 Thermal Imaging System:

Infrared cameras and thermal imagers record images using infrared (IR) radiation rather than the visible light used by traditional cameras [25]. Infrared cameras are sensitive to wavelengths between 1 and 14  $\mu\text{m}$ , much beyond the visible spectrum's 400-700 nm range. The use of an infrared camera allows for the capture of detailed video or stills that would otherwise be invisible to the naked eye [26]. Since rocket engine exhaust has high emissivity in the infrared spectrum, an infrared camera may be used to better describe.

Images captured by infrared cameras highlight characteristics of the plume, such as its structure [27], turbulence, and shock. Many factors, such as the motor's operating circumstances, the propellant's composition, and the motor's design, can alter the plume's irradiance characteristics. Considering that aluminum is a common component to solid rocket fuel [28], it is fascinating to examine IR photographs of the plume from a solid rocket engine and see how the structure of the plume and its properties alter with the amount of aluminum in the propellant. As has been discussed, alumina is created when particles in the plume react with those in the air.

Infrared light has a hard time penetrating alumina because of the material's high reflectivity and poor emissivity [29]. In Figure.5. show the real image takes by visible light television camera for a solid propellant fuel. Figure .6. show the thermal imaging camera and analysis of temperature of exhaust solid propellant fuel [30]. In Figs 5 and 6, the combustion of the solid propellant is depicted in the visible and infrared spectrum. It is noted that thermal imaging gives an accurate analysis of the temperatures of the combustion product. This information is very important to know the combustion efficiency of solid fuels.

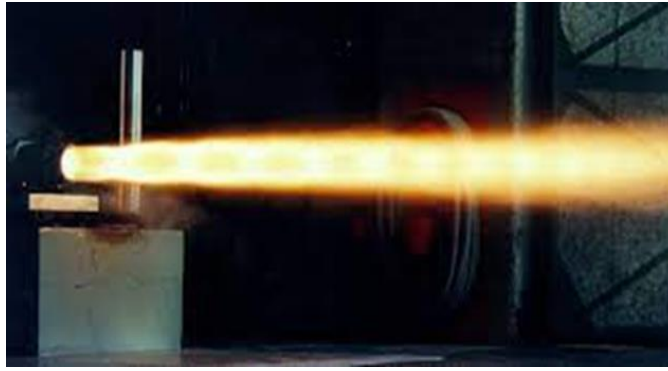


Fig.5. the real image of TV camera for exhausts solid propellant fuel

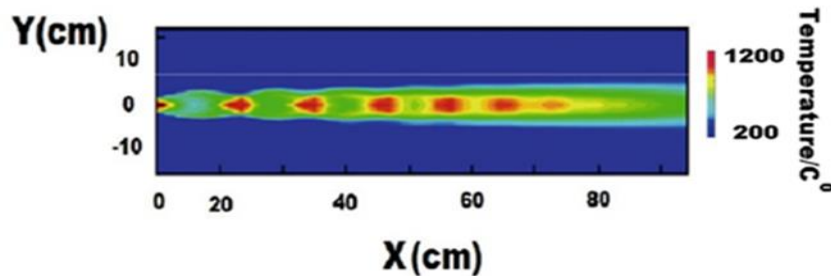


Fig.6. the thermal imaging camera and analysis.

One of the major drawbacks of this technology. Imaging inaccuracy, resulting from thermal reflections surrounding the sample to be photographed. Imaging accuracy tolerance  $\pm 2\%$ . It is also not as accurate as measurement systems directly connected to the sample to be measured thermally [31].

## 2.4 Shadowgraph Technique and Systems:

Since the 17th century, Schlieren has been used to depict the unseen with "white" light [32], and to describe high-velocity flows such as those found in the combustion of a solid rocket column. Optical methods reveal refractive noise in a transparent medium using lenses, mirrors [33], and cameras.

The shadow created on the screen during visualization as a result of the density of the liquid is what forms the basis of the shadow drawing technique [34]. Shadowgraph Photography Highlights When two different mediums meet, a change in refractive index occurs Non-reflective light from behind the object or backlight There will be background luminous due to this item, while the light the facade is full of holes, and as a result it looks dark shadow images consist of dark areas on the foreground and a lighter area in the background where the refraction varies. For the most part, shade should only be used when it is the media to analyze is transparent and designed to hold large amounts of data. Differences in refractive index (air and water). Although this method's underlying visual concepts are straightforward, it is not always amenable to straightforward laboratory implementation [35]. The simple nature of the design is reflected in the shadow system. However, there are a great deal of factors that need to be They are controlled and manipulated to create pictures that are of any value for analysis. All Shadowgraph systems share a same structure, albeit their individual parts are unique [36]. Figure.7. general schematic diagram of shadowgraph technique.

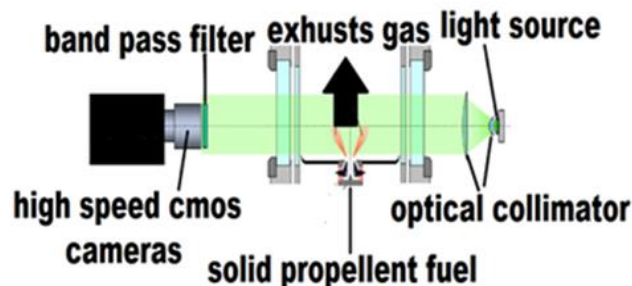


Fig.7. general schematic diagram of shadowgraph technique.

The system consists of a light source, an optical system for collecting beams, a number of two windows at the interstitial space of the solid fuel, and on the other side a CMOS camera [37]. Which gives a picture of the shape of the combustion exhaust of solid fuel and standing in the form of the combustion product to measure the capacity and efficiency of its combustion. In Figure.8. the real image shadowgraph exhausts of solid propellant fuel [38].

The images that were produced by using this technology in order to see the shape of the flame are presented in Figure 8. This method has a number of benefits, one of which is that the light emitted from the observed phenomena does not affect the image [39], and thus we get a good picture that accurately shows us the shape of the exhaust and the measurement of the basic specifications for it. Here, for example [40], the dimensions of the flame resulting from the combustion of the fuel are determined, and let the previous sample be 1.5 mm, thus allowing us to calibrate the combustion. The main drawback of this technology is that it has low sensitivity in combustion operation of rocket fuel, especially at the beginning of combustion in the presence of a shock wave. [41].

### 2.5 Digital Inline Holography (DIH):

All the methods have been covered so far center around some form of picture capture and analysis [42]. In conventional picture capture, light intensity is the physical quantity of interest. The DIH-based holography can simultaneously capture the front wave's phase and amplitude. The name "holographic," originating from the Greek for "writing" all information about a light wave, describes the way in which more data can be collected than is possible using traditional image collection methods. By splitting coherent light (emitted by a laser) into two beams, one illuminating the object under investigation and the other creating a reference, holography allows a person to record information about amplitude and phase and create a 3D visualization of the object., holography attempts to recreate the wave front that originated from it. The interference pattern is impressed on the recording medium while the item is there, and the 3D picture is reconstructed in the same location after the object is removed from the setup provided that the lighting ray is the same as the reference ray, as is the case with optical holography.in Figure.9. general diagram of DIH technique [43].

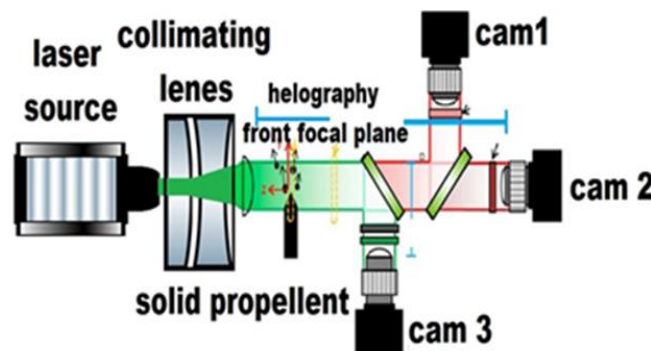


Fig.9. general diagram of DIH technique.

The DIH system consist of laser source 532nm has a pulse duration 5 nsec, collimating lenses group, three cameras and holography front focal plane [44]. This system is considered better than the previous systems, but rather one of the latest effective technologies in measuring the exhaust emissions of solid rocket engines, so it is working and reliance on its results to evaluate the performance of the fuel, but the system is flawed by complexity and signal processing systems that do not work in real time but rely on image storage and processing with processing technology.

The signals are in a complex style and the cost is relatively high than its previous counterparts. The main drawback of this technique is the use of software algorithms to create a three- dimensional image that distorts the image. In the case of images taken from different cameras with no near-instant synchronization.

### 3. Methodology of A Comprehensive Optical System Design:

All of the previous systems discussed, including DIH, run on a small, solid sample of rocket engine fuel, to avoid damage system, and this is a lab test rather than field measurements. the judgment of a complete rocket engine is difficult. Therefore, it was thought to design and implement a system that works in field tests without damage and with high efficiency. It is the best solution for evaluating the actual performance of missile engines.in Figure.10.the general block diagram of a proposed optical system. The proposed comprehensive optical diagnostic system consists of an ND-YAG laser source, which is a solid-state laser with a wavelength of 1064 nm, which is powered by a pump-source flash lamp , there is an optical system to make an angular divergence that can be adjusted after the laser source,

according to the distance of the source from the exhaust of solid rocket fuel combustion, There is also a thermal camera next to the laser source to photograph the combustion exhaust in a way that shows the exhaust temperature while giving an accurate shape of it , On the other side of the rocket engine, there are two high-speed CMOS cameras between them, a bidirectional separator that splits the beams between the two cameras evenly in order to make a three-dimensional image of the combustion product. They are also equipped with two systems for collecting beams that can be adjusted according to the distance between them and the laser source [45].

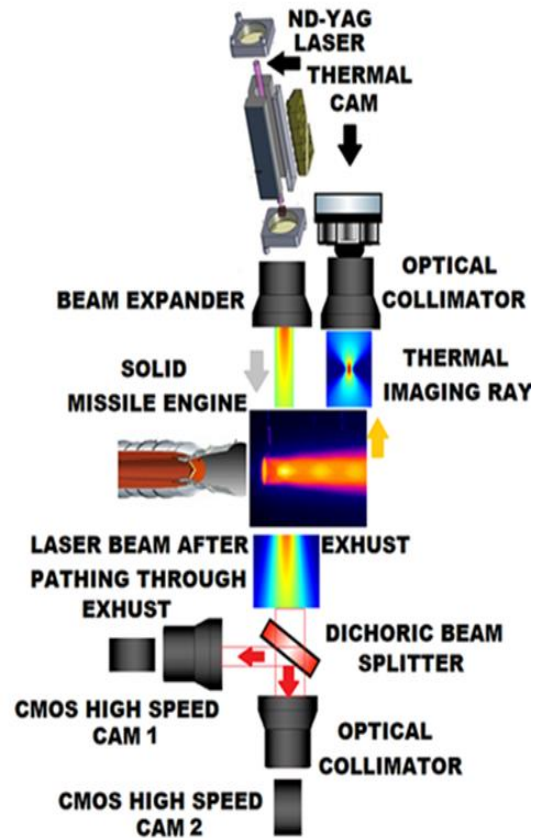


Fig.10. the general block diagram of a proposed optical system.

### 3.1 Design of ND-YAG Solid State Laser Source:

The solid-state laser consists of the active medium, pumping source, power supply and two mirrors. Active medium: It is a crystal of a solid material into which active ions are introduced for the purpose of laser generation, the material is ND-YAG rode. The pumping source Mostly use flashlight or laser diode 808nm. the flashlight is shedding effort an electric current between the two ends of the flashlight produces rays of light that are absorbed by the active medium crystal to irritate [46]. Crystal can be pumped the effective medium is using another laser beam, such as a semiconductor laser, and this method is more efficient than the pumping method with flashlight.in Figure.11. show the proposed 3D design of ND-YAG laser.

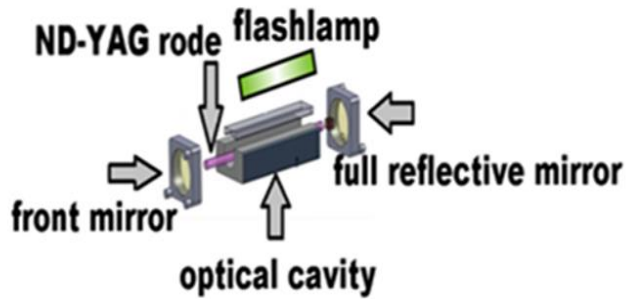


Fig.11.show the proposed 3D design of ND-YAG laser.

The ND-YAG laser consists of five main components which are the optical grommet, the flash lamp, two mirrors and the ND-YAG rode. The cooling system working in these laser systems is a water-cooling system. Calculations of electrical flash lamp pumping source in the following equations. the electrical discharge voltage according to equation (1) [47].

$$V = K_o I^{\frac{1}{2}} \quad (1)$$

Where  $K_o$  is a constant amount called the constant of the impedance properties of the strobe lamp and its units ( $\Omega \cdot A^{1/2}$ ). Its value is given as follows equation (2).

$$K_o = K \frac{L}{d} \quad (2)$$

Where  $K$  Constant depends on the type of gas used inside the flashlight and  $L$  The distance between the electrodes of the electric discharge inside flashlight and  $d$  the inner diameter of the strobe lamp. The value of  $K$  It is equal to (1.27) in the case of the xenon lamp at pressure (450 Torre). In the case of another pressure, the relationship is as follows equation (3).

$$K_o = 1.27 \left( \frac{p}{450} \right)^{0.2} \left( \frac{L}{d} \right) \quad (3)$$

( $t_r$ ) Rise Time takes a while for a flashlight voltage or current to rise from zero to its maximum value It is given as follows equation (4).

$$t_r = \sqrt{LC} \quad (4)$$

Where  $L$  and  $C$  Expanded charging capacity, the total time of the flash lamp pulse  $t_p$  It is given as follows equation (5).

$$t_p = 3t_r = 3\sqrt{LC} \quad (5)$$

In Figure.12. the Xeon flash lamp descriptions in 2d scale. The specifications of the used flashlights are as follows inner diameter (10mm), And the distance between the poles (20cm) It contains xenon gas. by pressing (600torr), the electrical discharge voltage at which the lamp operates is (3kv), The electric discharge current becomes 334KA, the total time of the flash lamp pulse if the capacitance is capacitive (10 $\mu$ F) is (3msec), and inductive coil is (0.1H). the calculation as follows:

$$K_o = 1.27 \left( \frac{p}{450} \right)^{0.2} \left( \frac{L}{d} \right) = 1.27 \left( \frac{600}{450} \right)^{0.2} \left( \frac{20}{1} \right) = 26.9$$

$$\therefore V = K_o I^{\frac{1}{2}}$$

$$\therefore I = \frac{V^2}{K_o} = \frac{(3 \times 10^3)^2}{26.9} = 334 \text{ kA}$$

$$t_p = 3t_r = 3\sqrt{LC} = 3\sqrt{10 \times 10^{-6} \times 0.1} = 3 \times 10^{-3} \text{ s} = 3 \text{ ms}$$

Specifications of Rod ND-YAG Length 20 cm and diameter 10 mm the concentration of ions in the rod is  $(10^{22}; 10^{25}) \text{ cm}^{-3}$  This is called the vaccination rate. in Figure .13. show the real rod image. The power threshold needed to start laser working is given by the following equation (6) [48].

$$P_{\text{thr}} = \frac{h\nu_p}{\eta_p \sigma_{se}(\lambda_1)\tau} (T + L) \frac{V}{2d} \quad (6)$$

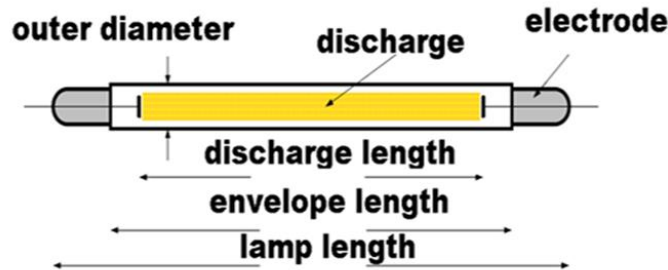


Fig.12. Xeon flash lamp descriptions.



Fig.13. real image of ND-YAG rod.

where  $h\nu_p = 2.54 \times 10^{-19}$  j is the energy of pump photon,  $\eta_p = 81\%$  is the pumping efficiency,  $\sigma_{se} = 2.8 \times 10^{-19} \text{ cm}^2$  is the stimulated emission cross section,  $\tau = 130 \mu\text{m}$  is the lifetime of the upper laser level,  $T = 5.1 \pm 0.9\%$  is the mirror transmission,  $\lambda_p = 808 \text{ nm}$  is the pump wavelength,  $L = 0.075$  is the passive losses in active medium,  $\lambda_1 = 1064 \text{ nm}$  is the laser wavelength,  $V$  is the pump volume,  $d = 20 \text{ cm}$  is the length of the laser crystal. the total efficiency can be written as follow equation(7)[49].

$$\eta = \eta_p \frac{\lambda_p}{\lambda_1} \frac{T}{T+L} \quad (7)$$

The total average power is 1 watt. in Figure.14. the 3D stereoscopic of a proposed laser cavity system and in Figure.15. the real image of a proposed laser system.

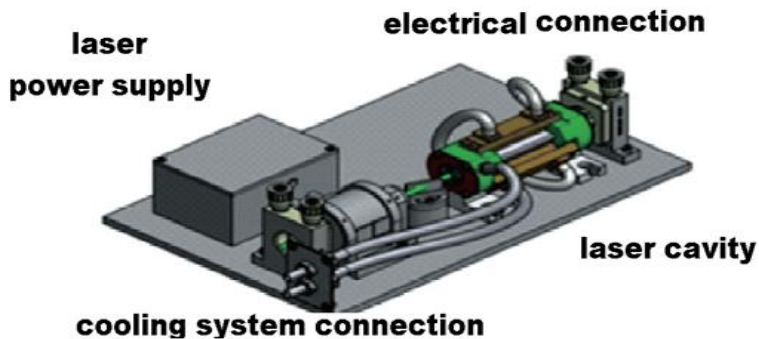


Fig..14. the 3D stereoscopic of a proposed laser system.

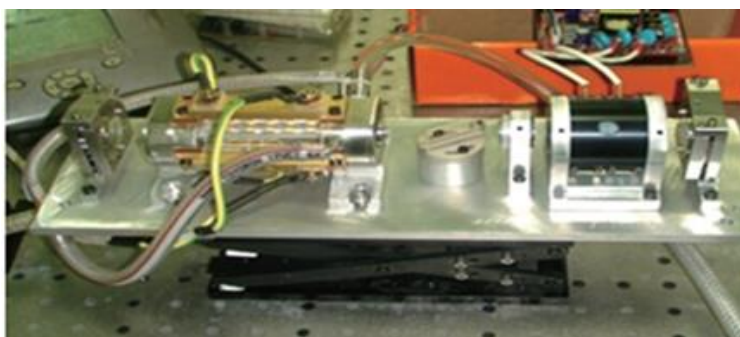


Fig.15. the real image of a proposed laser system.

The proposed laser system contains an optical system that increases the divergence angle by 1 mrad, the proposed expanded optical system consists of four lenses, the first lens is of the plan convex type, the second lens is the type of Plano concave lens, the third and fourth lenses are of the Plano convex type with a diameter greater than the first in order to meet the need for angular divergence required in Table No1. One containing the specifications of each from those lenses and the type of material they are made of it.in Figure.16. The 3D design of optical proposed system after ray tracing by winless 3D.and Figure.16. B show 2D design to show clearer.

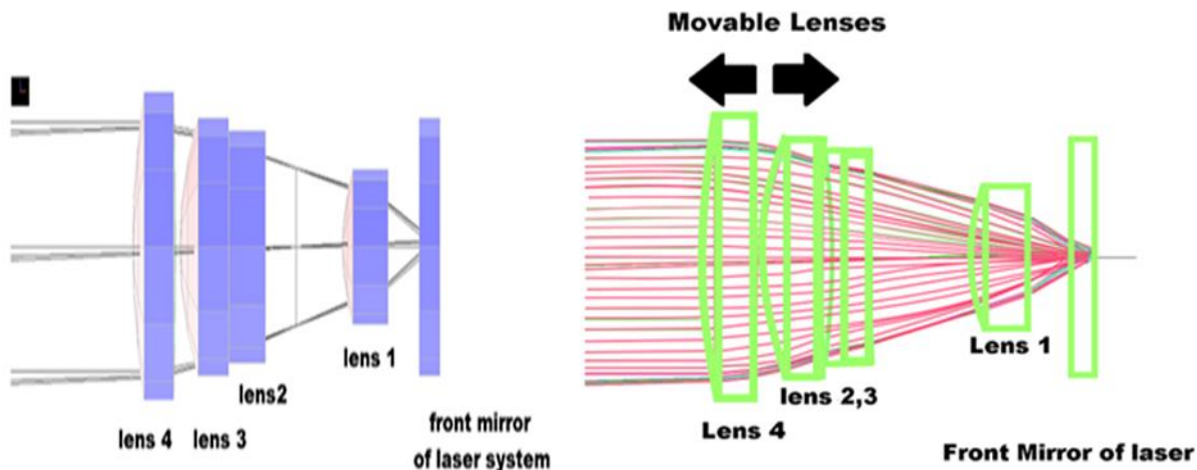


FIG.16,A,B . THE 3D AND 2D SCALE OF PROPOSED SYSTEM AFTER RAY TRACING BY WINLESS.

TABLE .1. TECHICHANICAL SPECIFICATIONS OF FOUR LENSES

Lens Number	Effective Focal Length	Numeric al Aperture	Lens Material	Clear Aperture (f)
1	8.0mm	.547	S-LAH64	7.71mm
2	0.0mm	.545	S-LAH64	9.88mm
3	12.0mm	0.546	S-LAH64	13.50mm
4	15.0mm	.534	S-LAH64	14.41mm

A simulated test for aberration factors was carried out using the ZEMAX program according to the following two equations (8,9) [50].

$$\varepsilon_x = S_1\rho^3\sin\varphi + S_2Y\rho^2\sin2\varphi + PY^2\rho\sin\varphi \quad (8)$$

$$\varepsilon_y = S_1\rho^3\cos\varphi + S_2Y\rho^2(2 + \cos2\varphi) + (S_3 + P)Y^2\rho\cos\varphi + S_5Y^3 \quad (9)$$

where  $\varepsilon_x$  is the Seidel aberration in the  $x$  axis direction,  $\varepsilon_y$  is the Seidel aberration in the  $y$  axis direction,  $S_1$  is the spherical aberration,  $S_2$  is the Coma,  $S_3$  is the astigmatism,  $P$  is the Petzval sum,  $S_5$  is the distortion,  $Y$  is the ideal image height on the image plane,  $\varphi$  is the ray of angle position at the exist pupil, and  $\rho$  is the ray height at the exist pupil. in Figure.17. Seidel's chart to each surface of four lenses separately by ZEMAX.

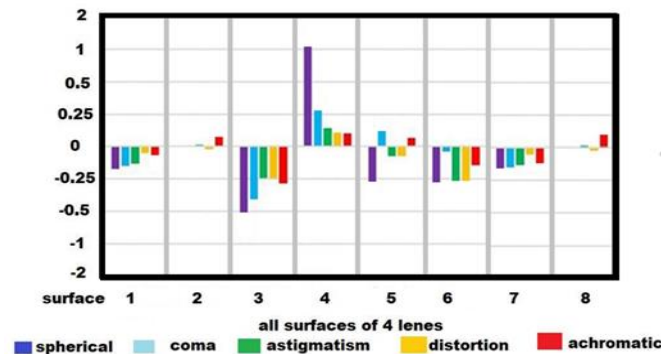


Fig.17. Seidel's chart to each surface of four lenses separately by ZEMAX.

Commenting on the results of the optical analysis of the five optical aberration coefficients in that figure, the most important values for coma and distortion coefficients are due to their significant effect on the laser beam radiation, and so that the shape of the laser spot is formed in a symmetrical Gaussian shape, so the values shown in the figure are considered small values that do not affect the idealness of the laser radiation in a way Gaussian shape as will see in the next 3D drawing. Simulate the shape of the laser beam after laser passing through the optical system. Its perfect Gaussian beam propagation, the laser beam spot size is calculated. When modelling the intensity distribution of a Gaussian beam, it's a collection of rays, where the direction of each ray is erroneous by some random amount. The typical geometrical optics formulas are used to allow the ray bundle to pass through the proposed optical system, and it is demonstrated that the location of the focused beam waist agrees exactly with the typical Gaussian mode analysis in. The spot size of the beam along the propagation  $z$ -axis is then determined by the parameters of the Gaussian mode. Figure.18. laser beam profiling after pathing through the proposed optical system.

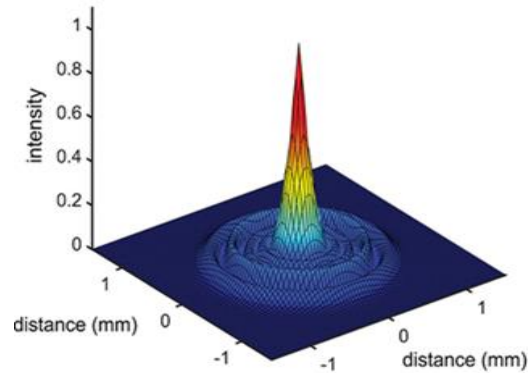


Fig.18.simulating result of laser beam profiling after pathing through the proposed optical system

Since these parameters mentioned are low values, it is clear that the laser beam profiling is identical to the Gaussian shape, and as in the previous figure, those measurements were made with a laser beam profiling in laboratory test and under atmospheric clear conditions, away from dust and aerosols to determine the quality of the laser beam after passing through the proposed system Optical.in Figure .20 the real image of laser spot size and Gaussian shape distribution by using laser beam profiler . This is a practical experiment to determine the similarity of the simulation with the practical experiment and to measure the quality of the laser beam propagation. the laser beam profiler utilized SP932U Camera, the wavelength band from 190 to 1100 nm. The difference between the simulated result and the process result is that the simulation program works in ideal conditions, but when measuring the laser spot in real weather conditions in the field, some differences occur due to weather conditions. It is worth noting that the laser source must be 100 meters away from the solid fuel flame to avoid destroying the optical system of heat from combustion. Figure 19 shows 3d design of a proposed optical system expander of laser source in Figure .23. the optical hard ware implementation of the proposed optical system for the laser source. Complete visual alignment was taken into account in producing the final shape. The chassis of the proposed optical system has also been charged with nitrogen gas to avoid moisture, which in turn leads to the presence of unwanted fuzz in the optical systems.

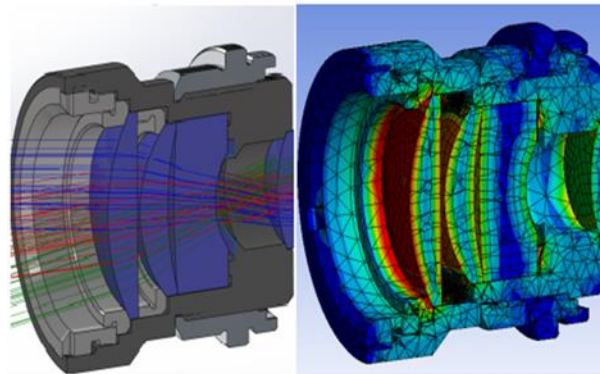


Fig.19. 3d design of a proposed optical system expander of laser source

In the case of any multi-lens optical system, the primary function of that system must be considered. On this basis, the optical design of each lens is worked out separately, as well as the distances between the lenses [51]. The following has been calculated for those factors affecting the distances between lenses according to the field of the opto-mechanical system in Fig.20. View the parameters of the distance lens system between them.

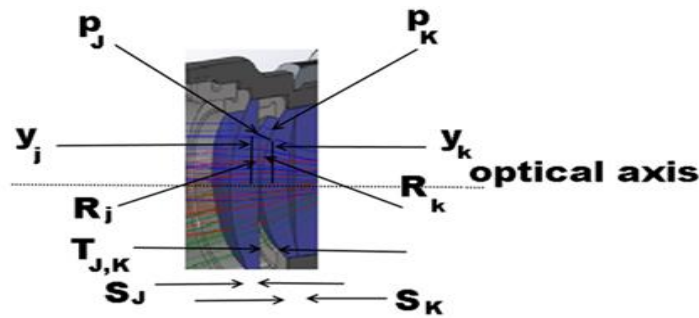


Fig.20. View the parameters of the distance lens system

These factors shown in this Figure are given by the following equations (10,11,12) [52].

$$S_j = R_j - (R_j^2 - y_j^2)^{1/2} \quad (10)$$

$$S_k = R_k - (R_k^2 - y_k^2)^{1/2} \quad (11)$$

Where  $L_{j,k}$  the distance between two point  $P_j$  and  $P_k$  at heights  $y_j = 24.384$  mm and  $y_k = 21.946$  mm in the surface of lens radius  $R_j = -74.778$  mm and  $R_k = +69.088$  mm and  $T_{j,k} = 4.978$  mm is the distance between two lens and the sagittal depths are  $S_j = -4.088$  mm, and  $S_k = 3.578$  mm. in this case the distance between two lenses is :

$$S_j = -\{74.778\text{mm} - [(74.778\text{mm})^2 - (24.384\text{mm})^2]^{1/2}\} = -4.088\text{mm}$$

$$S_k = \{69.088\text{mm} - [(69.088\text{mm})^2 - (21.946\text{mm})^2]^{1/2}\} = 3.578\text{mm}.$$

$$L_{j,k} = 4.978\text{mm} - (-4.088\text{mm}) + (+3.578\text{mm}) = 12.649\text{mm}.$$

Thus, the distance between the third and fourth lens was calculated because that distance is controlled according to the angle divergence of the laser beam. the distance between the first and second lens is fixed 5 cm. The distance between the second and third is zero, meaning that the two lenses are attached to the optical resin epoxy in Figure.21. optical implementation of proposed optical collimator.



Fig. 21. the optical hardware implementation of the proposed optical system

### 3.2 Thermal Camera and Optical Collimation Unit:

The types and features of any obtainable thermal camera vary, ranging from only basic capabilities to superior reading and comparison capabilities. As for the image displayed by the camera [53], it is divided into two main parts: the black and white display and the spectrum display, also known as the rainbow spectra display. The first type of black and white display was used to define more details in the image. As for the spectral display, it is used to display the differences between different temperatures and is the most sensitive to thermal energy. Some types of thermal cameras also include a set of advanced specifications, such as determining a certain temperature, whose elements are displayed only without other [54]. It is also possible through some cameras to display an image within a picture with different spectra, and some other cameras, allow the possibility of combining different temperatures and displaying them in a uniform color. All of these properties can be used in different applications of this type of thermal imaging. Choosing the most suitable thermal camera, there are a number of elements through which it is possible to select the most suitable thermal camera, which is related to the quality on the one hand, and the price and cost of the camera on the other hand, among these elements, there are two very important elements, which are the accuracy of the display of the camera screen and its sensitivity to heat [55].

The Thermal camera screen display resolution describes the number of pixels you display, and the most common and common display resolutions are 160×120, 320×240, 480×640. for example the accuracy of 240×320, Displays an image consisting of 76,800 pixels. Which means 76800 temperature data points where each pixel individually displays a specific energy data, which of course means that, the more Resolution, higher quality and detail of the image on the one hand, and the higher value of the thermal data captured on the other. The other important parameter is sensitivity of the camera to heat, it indicates the minimum temperature difference that the camera can detect, which means that the sensitivity of 0.05 degrees means that the camera can differentiate between two temperatures by 5/100 degrees, another factor influencing your choice is the camera's temperature range, which is the range between the lowest and maximum temperature the camera can capture. The ideal range is 4 to 2200 degrees Fahrenheit. According to what was previously mentioned about how to choose the thermal camera in terms of accuracy and sensitivity to temperature, this camera was chosen to suit our need to photograph the burning of solid rocket fuel, (ThermoView TV40). in Figure.22. Show the real image of TV40 thermal camera. The ThermoView TV40 is a high-performance industrial fixed thermal imaging system that provides continuous infrared and visual feeds to display temperature data, hence increasing comprehension. The TV40 provides an all-in-one system for temperature regulation, tracking, and record keeping.



Fig.22. the real image of TV40 thermal camera.

The tough TV40 thermal camera's dependable, excellent 320x240 and 640x480 infrared resolution options to enable view of the temperature data you need every several crucial aspects. The technical specification of TV40 in table.2. in addition, the display program of this camera enables us to: Communications with Multiple Cameras simultaneously view thermal and visual images. (IR-Fusion) capable of DAQ (I/O) communication User-defined condition settings and advanced analytics settings for alarms and unrestricted areas of interest automatic identification of lenses (Field interchangeable lenses) Export Images & Graphs as PNG, JPG, TXT, CSV, and AVI.

The second part of the optical system of the thermal camera, that system consists of five lenses and a glass dome. This optical system collects spectral rays in the near and medium infrared range in order to help the camera to form a high-resolution image in addition to addressing the distance between the place where solid rocket fuel is burning and the place where the thermal camera is installed. Figure .23. A shows the shape of the optical system using the Win lens 3D program. In Figure 23.B a two-dimensional drawing was made to show the shape and type of lenses used without the optical dome, and the type of each lens was written in order to find out the details of the design with ray tracing of a single wavelength in near IR.



Fig.23.A, B. the optical system design using the Win lens 3D and 2D program.

Table.2. technical specifications of TV40

Feature	Description
<b>Sighting</b>	Thermal Imager + Visible Light (320 x 240 or 640 x 480)
<b>Measuring Range</b>	2: -20 to 1200°C (-4 to 2192°F)
<b>Measurement Accuracy</b>	±2°C or ±2% (reading)
<b>Image Resolution</b>	320 x 240 (76,800 pixels) & 640 x 480 (307,200 pixels)
<b>Field of View</b>	Horizontal 34° x 25.5°
<b>Spectral range</b>	8 - 14 μm
<b>Detector</b>	Uncooled detectors array

Since the proposed optical system for the TV40 camera is an optical system dedicated to creating images that differs

from the optical system of laser systems as in the past. it is necessary to check the path of the rays passing through the optical system, this was done with the ZEMAX program, as in Figure .24. The ZEMAX program gives an accurate analysis of the path of the incident and passing rays of the optical system dedicated to the cameras in an image that is very close to reality. so, it is considered one of the best design programs for optical systems for creating images with high accuracy. The main reason for putting this design in this way is to collect as much radiation as possible to do a spectral analysis of the combustion missile fuel.

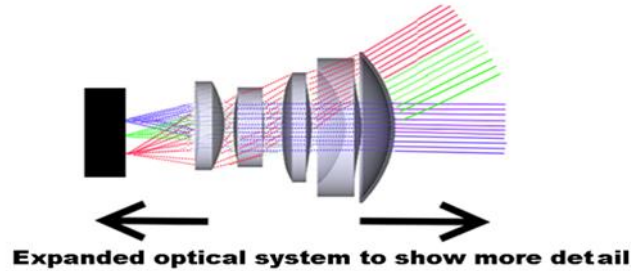


Fig.24. the optical proposed system expanded by ZEMAX with raytracing

the exhaust that comes out, and to measure its temperature from a distance of 100 to 1000 meters, With a 60-degree field of view. Also, optical zoom has been placed in order to create an image with a wide stereo width. The specifications of that optical system are shown in the following table .3.

Table.3. Technical specifications of five lenses

Lens Number	Effective Focal Length	Numerical Aperture	Lens Material	Clear Aperture (f)
1	16.0mm	.647	SF-18	7.71mm
2	2.0mm	.5475	SF-18	9.88mm
3	5.0mm	0.396	SF-18	13.50mm
4	3.0mm	0.234	SF-18	14.41mm
5	1.05	0.06	SF-18	5.00654mm

The glass dome is very important in this application due to two main factors, the first is to protect the optical system from the potential pressure resulting from the exhaust of missile fuel, despite the distance of the optical system from the place of combustion, and the second reason is the display of the radiation stereotype that reaches 180 degrees according to the design of the optical system located after the glass dome.in Fig.25. show the optical proposed glass dome design analysis by Ansys. Ansys program was used to calculate the loads on the optical dome, which is a distinct program in those calculations, as it puts the basic inputs to simulate conditions that simulate the truth and make semi-accurate calculations, to determine the quality of the optical dome in different weather conditions of pressure and temperature. It is worth mentioning that the optical dome is made of ZnSe material. At the front of the optical system, a ZnSe dome is simply supported with a radius of  $r = 50$  mm. The angle of the top of the dome is 60 degrees. The approximate minimum thickness of the dome using the fracture resistance  $Y_S = 50$  MPa and  $SF = 4$ . Stagnation pressure on the dome as follow equations [56].

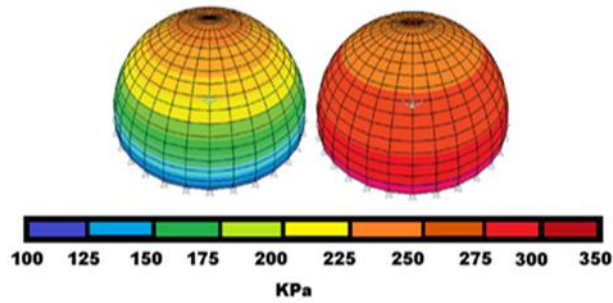


Fig.25. optical proposed glass dome design by ANSYS program.

$$\frac{P_{st}}{P_{\infty}} = \left( \frac{\gamma+1}{2} M^2 \right)^{\frac{\gamma}{\gamma-1}} \left( \frac{2\gamma}{\gamma+1} M^2 - \frac{\gamma-1}{\gamma+1} \right)^{-\frac{1}{\gamma-1}} \quad (13)$$

Where  $P_{st}$  the stagnation pressure  $P_{\infty} = 26.4\text{kPa}$  function of the ambient pressure  $M^2$  dimensionless flight Mach number  $1 \leq M \leq 5$  and  $\gamma$  is the specific heat ratio ( $\gamma \approx 1.4$  for air).

$$P_{ST} = 26.4\text{kPa} \left[ \frac{1.4+1}{1.4} (3)^2 \right]^{\frac{1.4}{1.4-1}} \left[ \frac{2(1.4)}{1.4+1} (3)^2 - \frac{1.4-1}{1.4+1} \right]^{\frac{1}{1.4-1}} = 318\text{ kPa}$$

According to the calculations indicated from Equation No. 13, the pressure on the dome of the designed optical system was calculated is 318 kPa. It is noted that the simulation program reaches a pressure of 350 kPa, and this pressure is considered the maximum pressure that the dome can withstand and then collapse after that. As for the chassis design, the design was done using SolidWorks program. Figure 26 shows the chassis design with the protective dome of the optical system of the TV40 thermal camera.

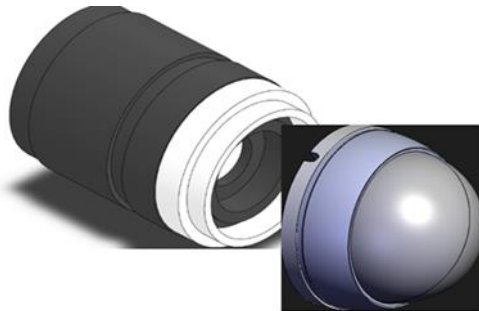


Fig.26. the chassis design with the protective dome of the optical system

In Figure 27 it shows the real picture after the completion of manufacturing the optical system, placing it in the chassis and installing the protective dome for it with the work of the optical alignment. The aberration coefficients required for that optical system were also measured by measuring the Seidel aberration in the  $x$  axis direction,  $\varepsilon_y$  is the Seidel aberration in the  $y$  axis direction show in Figure .28.



Fig.27. the real image after the completion of manufacturing

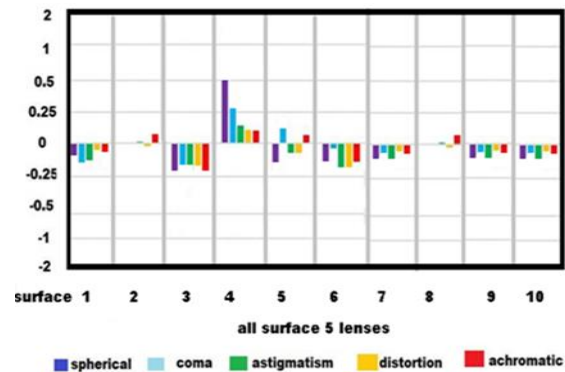


Fig.28. Seidel's chart to each surface of five lenses separately

According to previous experiences in this field, these results are considered to be very distinctive, as the optical system that makes up the image must reduce the aberration coefficients to the maximum degree, especially achromatic and distortion aberrations confident to create an image free from color distortions and unwanted interference ray tracing. It is also noted that the sum in the positive and negative direction after finding the resultant difference for all types of deviation coefficients leads to a very small value that leads to zero.

### 3.3 Dichroic Beam Splitter Design and Implementation Beam splitters find their most common use in optical

System and laser spectroscopy applications including storage and fluorescence Interferometry, a type of semiconductor device in which a portion of the optical signal being sent must also be reflected. Light is divided by a percentage when it passes through various layers, and it is achieving effects by Density or wave length scale. In this research paper, the design and implementation of a dichroic optical beam splitter was done using two triangular prisms at an angle of 90 degrees' perpendicular to each other and glued to a high-strength and highly transparen optical resin epoxy, with a maximum transmittance at the wavelength near infrared 1800 nm to 2500 nm, its equal 85% to 90% [57]. In Figure.29. show the dichroic beam splitter by 3d design.

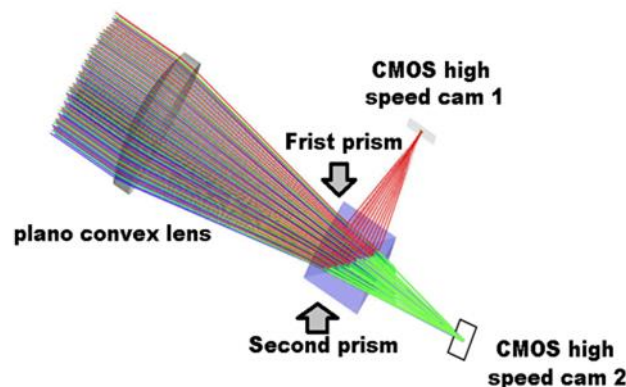


Fig.29. the dichroic beam splitter by 3d design software

It is noticeable that there is a Plano convex lens to gathering the emission rays from the exhaust of solid fuel when, its burning. The specifications of this lens are, effective focal length is 20.6, numerical aperture is 60.9, lens material is sk17, clear aperture is 6.9. the dichroic beam splitter Is characterized by Creating an image of the object to be photographed on a spectroscopic basis. Where the thickness of glass and type of the material of the vertical triangular prism is made adjusted for that purpose. The thickness is 0.345 and material is NBK7. The cut off  $\lambda = 740$  nm, Transmission Band 400: 725nm reflection band 750: 935 nm. In Fig .30. show the relation between transmission, reflectance and wavelengths band.

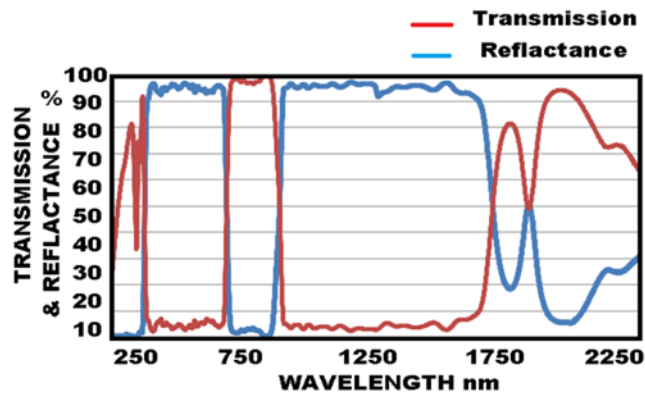


Fig.30. relation between wavelength and transmission, reflectance

Commenting on this figure, it is noted through the relationship between wavelength, transmittance and reflectivity the following ( $T > 97\%$ ) and ( $R > 93\%$ ) respectively. From all the above-mentioned specifications of the optical system dichroic beam splitter, it is clear that the system fulfills the purpose. As the system works to form two images of the same object at different wavelengths, then sends those images to CMOS high speed CAM. It is worth noting that this optical system provides complex computing operations based on image processing this saves time to work in real time [58].

In Figure.31 and 32. It shows a real picture of the optical system of dichroic beam splitter where the two perpendicular prisms were placed from the base, in a chassis charged with nitrogen gas to protect the optical system from the weather conditions operating in the experiment.

In Figure.32. shows the final form of the optical system, where there is 1 input of the aforementioned lens and a number of two outputs of fast cameras working on the formation of the three-dimensional image and analysis of the exhaust of solid rocket fuel. The chassis is made of processed aluminum. And compressed from the inside with nitrogen gas to avoid damage to the optical system when used during the experiment.



Fig.31, 32. the two perpendicular prisms were placed from the base and different view chassis of dichroic beam splitter charged with nitrogen

### 3.4 Two CMOS High Speed Cameras

The cameras that are used to take pictures of fuel combustion products are generally of a special type called high speed cameras, as they must have several special specifications, from the rate of images captured per second, the number of pixels, the type of lenses used to determine the field of view, their control systems. The image processing programs used with them. the minimum requirements are sCMOS  $2048 \times 2048$  pixels,  $7.4 \mu\text{m}$  pixel pitch, 14-bit depth, with 700 and 905 nm filters. Note the both have a full width at half maximum is 10 nm. If more than one camera is used, a 15-microsecond synchronization must be done between them, As in the proposed design. Accurate timing and minimal transmission line are requirements for the two pyrometer cameras. in Figure.33. the different view of high speed camera.



Fig.33. the different view of sCMOS high speed cam

Technical specifications of the camera to be used in that optical system, resolution by pixels = 2048 x 2048, pixel size= 11 x 11 microns, imaging area= 22.5 x 22.5 mm, sensor diagonal= 31.9 mm, maximum frame rate= 48 fps, cooling 45°C Below Ambient and Dynamic Range is 96 dB. It is worth noting that one of the most important calibrations of camera sensors used in spectroscopy and image formation. It is the quantum efficiency. It is a measure of the efficiency of converting photons into electrons. In Figure.34. the relation between wave length and quantum efficiency of this camera.

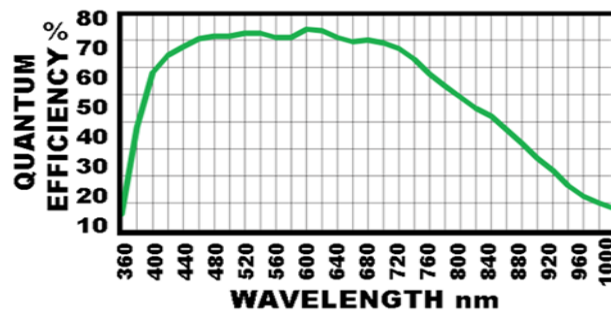


Fig.34. the relation between wavelength and quantum efficiency of camera sensor.

It is noted that the highest conversion efficiency between the photons falling on the sensor and the resulting electrons is in the region between wavelength 400 nanometers to 900 nanometers, which is completely required for this application. The second part of the cameras system for monitoring the exhaust of solid rocket fuel, it is optics group that gathering the outgoing rays Dichroic beam splitter. This group also has another function, which is that the sensor of camera does not saturated by radiation resulting from exhaust, which negatively affects the image formed and even destroys it. Therefore, it is placed at a distance of 10 mm from the sensor. In Figure .35. the 3D design of a proposed camera with optical system. The optical system consists of three lenses and a tightly-sealed aluminum chassis. In Figure 36 there is a detailed three-dimensional drawing of the optics group and its components as follows: lens barrel, 3lenses, spacers and threaded ring



Fig.35. the 3D design of a proposed camera with optical system

It is worth noting that the system has been designed very carefully to be compatible with the optical stage before it and the stage after it of sensors, and even the five deviation ratios were measured to ensure that their values do not affect the formation of the image well.

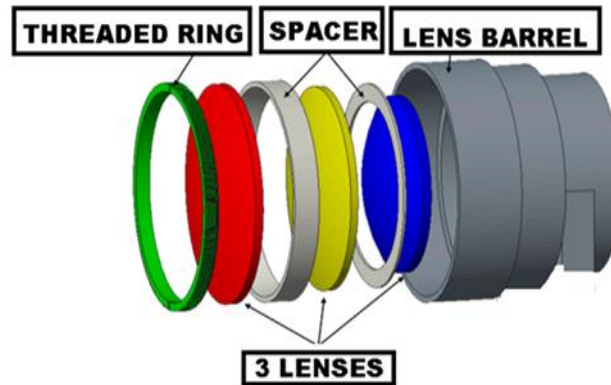


Fig.36. three-dimensional drawing of the optics group

In Figure.37 and 38. The optical design of the lenses is illustrated using the Win Lens 3D program 3d and 2d after ray tracing respectively. The optical system consists of three lenses that gathering the rays coming out of the aforementioned optical system. It produces a very clear image of the fuel combustion exhaust. Table 4 contains the technical specifications of the lenses. A measurement of the five aberrations coefficients was made. It was clear from this that the sum of those values according to the deviation equations is relatively small, which makes the visual system for it. It has the ability to form a clear picture of the radiation falling on it from the year of solid propellant fuel.in Figure .39. show the five sides aberrations chart.

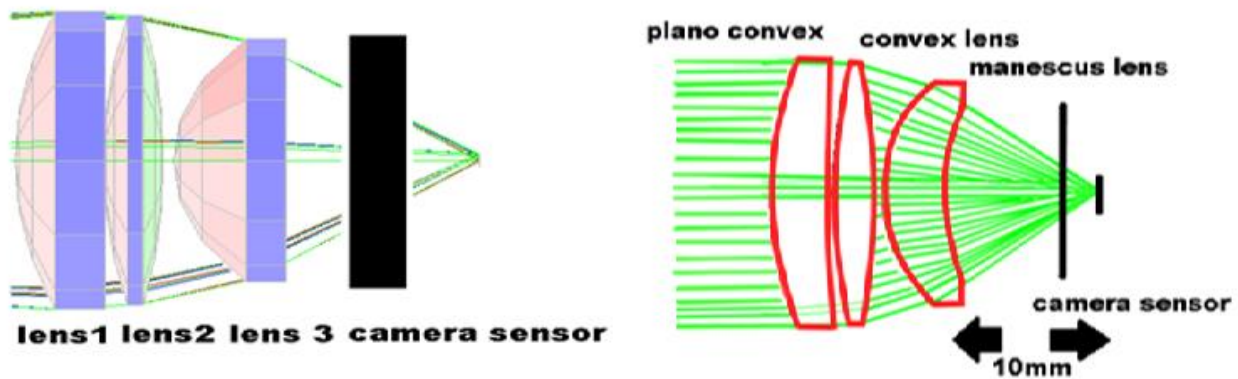


Fig.37 and 38. The optical design of the lenses is designed by the Win Lens 3D

Table.4. Technical specifications of five lenses

Lens Number	Effective Focal Length	Numerical Aperture	Lens Material	Clear Aperture (f)
1	7.56mm	.347	SK-7	10.71mm
2	5.0mm	.1475	SK-7	8.88mm
3	3.0mm	0.296	SK-7	6.50mm

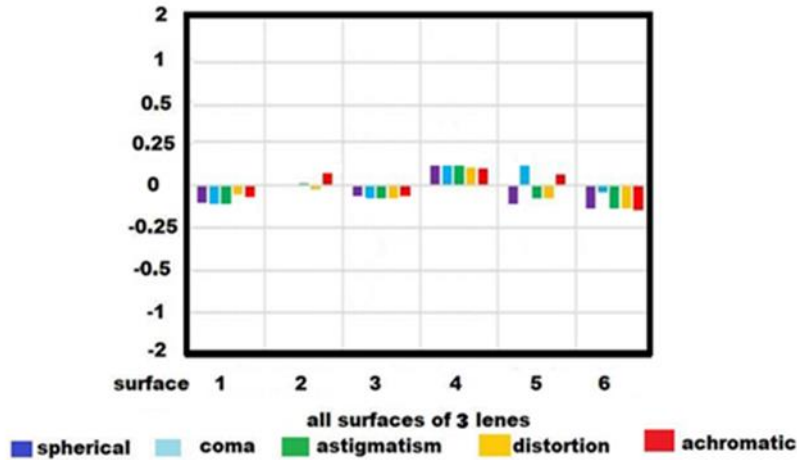


Fig.39. Seidel's of three lenses

chart to each surface separately by

ZEMAX

In Figure.40. the real image of optical system after fabrication. The camera is installed after adding the optical system to a mechanical installation system. It has the ability to move in the vertical and horizontal planes to adjust the appropriate field of view according to the angle of incidence of the rays on axis and off axis.in Figure.41. show the opt mechanical system design by solid work to install the camera and optical system. It is noted in that figure that picture No. A is a mechanical system based on a movement in the horizontal and vertical plane, as the step is 1 mm. the pictures No. B, they are to install the camera and make the complete alignment of the system before work. the alignment has a very important role in the formation of the image to be captured.in Figure.42. the real image of opt mechanical system after fabrication.



Fig.40. the real image of optical system after fabrication.

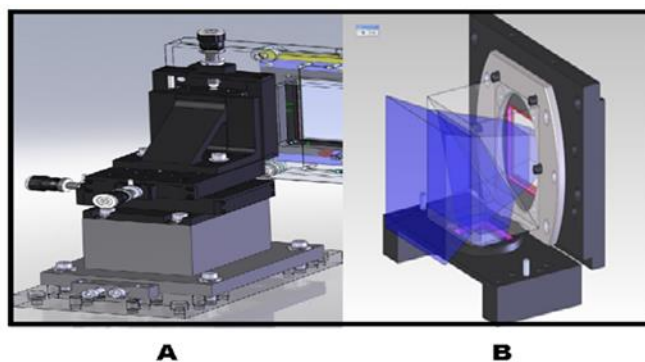


Fig.41. the opt mechanical system design by solid work to install the camera and optical system



Fig.42. the real image of opt mechanical system after fabrication

#### 4. Results

The experiments of the proposed system focus on imaging the rocket fuel exhaust from the moment of initial ignition to the end of the combustion process. The steps of the experiment are as follows in order. First, the proposed system is divided into two main parts. The first is for a laser source to illuminate the exhaust of missile fuel and a thermal camera for thermal imaging to give an accurate picture of the ignition shape and exhaust temperature. The second section is a double optical divider system with two cameras for three-dimensional imaging to discover the solid parts resulting from combustion, especially aluminum particles, their proportion and temperature with other gaseous exhausts.

The percentage of other gaseous emissions is inferred by the resulting radiation and its density determines the number of outgoing gases. Which gives the impression that the combustion is not complete or that the missile solid fuel system suffers from problems in manufacturing or storage. Placing the proposed optical system around the solid fuel column.

By placing the system divided into two parts in a perpendicular position to the combustion products, with a distance not to overturn each section and the combustion products for 100 meters for one solid fuel column. Designed for the rocket engine. But here we limited the experiment to only one column as an experimental sample.

The laser source was set to a pulse repetition rate of 45 Hz, which is an appropriate rate equal to the number of images taken by the camera per second. In Figure 43, an actual picture from the reality of the field trials of a rocket fuel engine with one fuel shaft. Figure.44. shows the image that was captured by the thermal camera after processing an image of the invisibility of the combustion product. So that the heat indicators for the engine body and the background were canceled to focus on the form of heat generated by the exhaust of solid rocket fuel



Fig. 43. actual image from the reality of the field trials of a rocket fuel engine

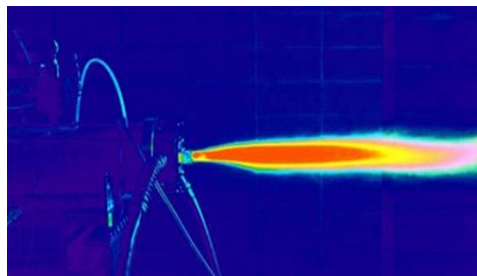


Fig.44. the image that was captured by the thermal camera TV40

Figure.45. shows the temperature gradient of the solid rocket fuel flame. Depends on the accurate analysis of the image of the flame resulting from combustion. Through the camera and the proposed optical group. It is worth mentioning that the role of the glass dome encased the proposed optical system has been demonstrated. it bears the constant pressure wave of the combustion resulting from the experiment.

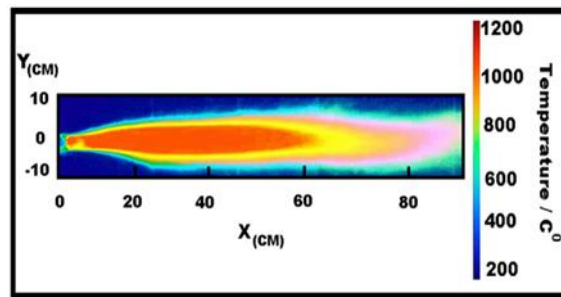


Fig .45. the temperature gradient of the solid rocket fuel flame

As for the gradation in the vertical direction, it is an expression of the diameter of the flame circle. As for the gradation in the vertical direction, it expresses the length of the flame for the sample of solid rocket fuel combustion. As for the thermal gradient, it starts from 200 degrees Celsius and ends with 1200 degrees Celsius, which is the temperature resulting from accurate image analysis using a custom processing system for thermal images. It was made specifically for that purpose. in Figure.46. by using a spatialize digital in line holography software program. This three-dimensional image was obtained from the interaction of the laser with the combustion products. This produced wavelength that fall in the ultraviolet spectrum at 350 nm to 900 nm in the near-infrared.

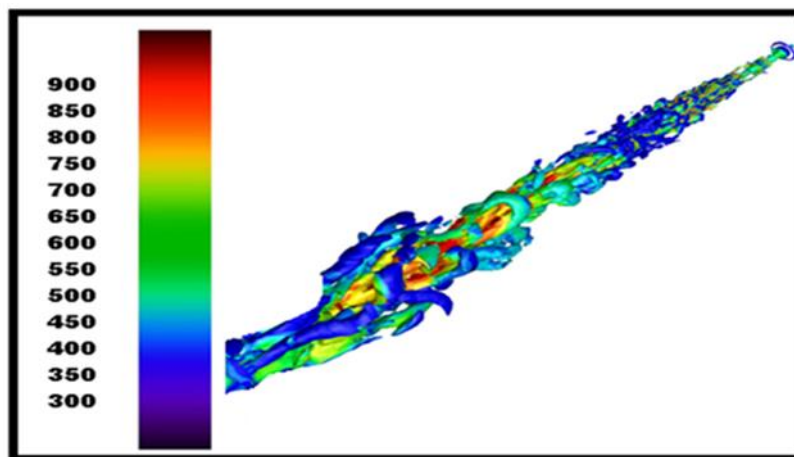


Fig.46. image of exhaust by using the two images of cameras after using spatial digital inline holography software

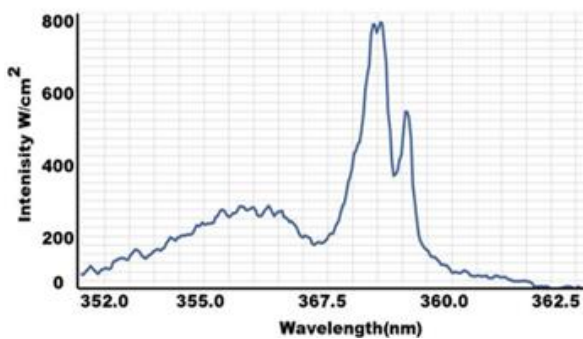


Fig.47. the spectrum of CN with emission intensity

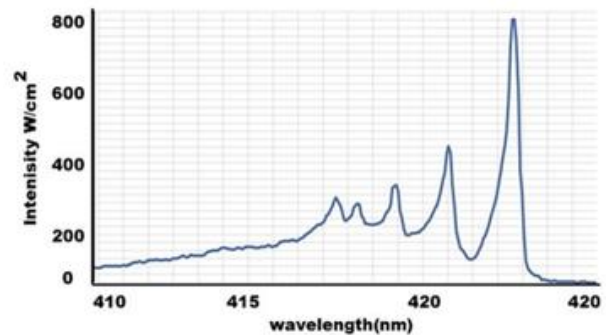


Fig.48. the spectrum of NH with emission intensity

The following figures show the laser's interaction with the various combustion products from the exhaust of solid rocket fuel, such as ,CN, NH, C2, CH, AL and OH.in Figure.47. show the spectrum of CN with emission intensity. The following spectra in Figures 48 ,49, 50 and 51 are second harmonic generation of the NH, C2, CH spectra under the experimental conditions of pressure, temperature, and exhaust and high flow velocity of solid rocket fuel. The most of the spectra of these compounds are confined between the near to medium infrared rays from 1 to 5 micrometers. they do not appear in the visible spectrum with wavelengths of value reminiscent, just in case of the stubborn burning and high temperatures and pressures. In the case of aluminum, the spectra remain the same because the volatile and dispersed aluminum particles in the exhaust products give the same analytical spectrum to them.

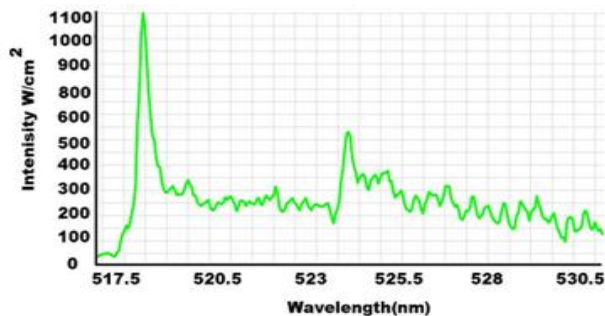


Fig.49. the spectrum of C2 with emission intensity

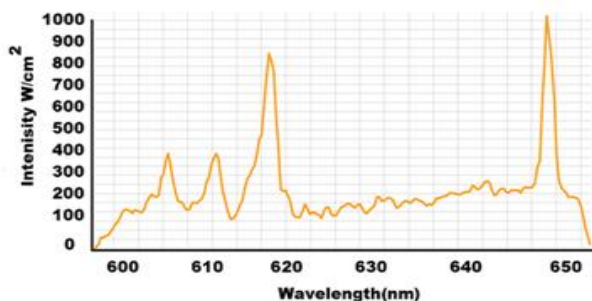


Fig.50. the spectrum of AL with emission intensity

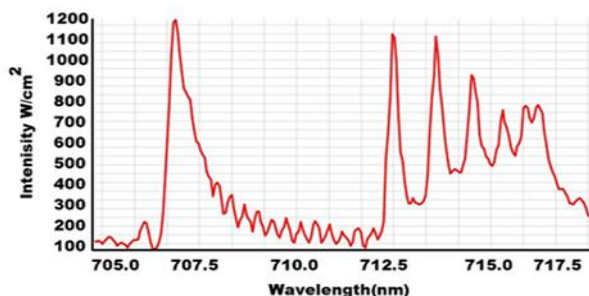


Fig.51. the spectrum of CH with emission intensity

The important role of the illuminated laser is manifested in illuminating the combustion products of the solid fuel flame. Especially the molten aluminum particles scattered throughout the exhaust, the image of the exhaust was taken before the laser source was turned on, and the result was unsatisfactory in detecting. aluminum particles. But after turning on the laser source, the aluminum particles appeared. In Figure.52. shows this process before and after turning on the laser source.

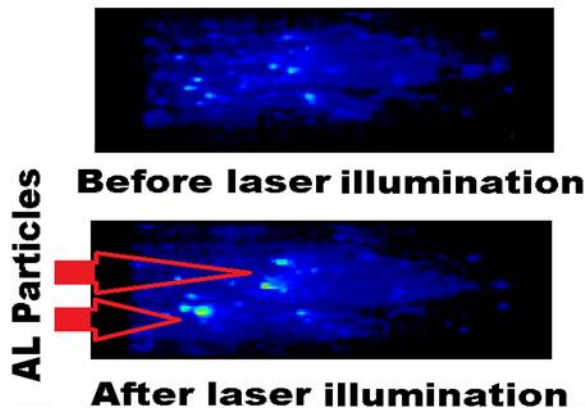


Fig.52. image of exhaust before and after laser source turned on.

By checking the parts in which the aluminum particles are located, it was possible to visualize them and determine their diameters and even the wavelengths emitted from them. The wavelengths emitted by a hot particle in a solid fuel flame depend on its temperature and its distance from the rocket engine nozzle. The optical system was able to photograph a sample of the particles and the imaging results were satisfactory. A number of particles with diameters of 120, 180 and 200 micrometers were detected. The discovery of such diameters means that the proposed optical system succeeded in performing the task for which it was manufactured. Figure 53 shows an accurate picture of aluminum particles in a solid rocket fuel exhaust flame. Also, the particles are placed on white circles to indicate them for the purpose of clarification.

The figure is divided into two parts, the first is a thermal image of particles, and the second is a near-infrared image and appears as a black and white image. Thus, the proposed spectroscopy system becomes a comprehensive system that gives accurate results on the combustion of solid fuels and the extent of combustion efficiency. The proposed system overcomes similar methods in spectral analysis alone. the main feature of the proposed optical system, the proposed optical system overcomes the defects of the previous techniques by ,1-The proposed optical system does not depend in measuring the exhaust products of combustion of solid rocket fuel, on a gas cell. Rather, the measurement is done remotely and not by taking a sample for analysis. 2-The proposed optical system works in the field atmosphere to test solid rocket fuel engines without affecting the surrounding environment. because the system is equipped with lenses made of special materials that operate at specific wavelengths.3-The thermal camera's optical system is equipped with a glass dome to work on, reducing reflections from the surrounding environment. Which in turn affects the thermal image formed

.4-The optical system is equipped with a laser source to illuminate the products of combustion. This is showing solid particles at the beginning of combustion in the presence of a shock wave. Which limits the effect of that wave on the quality of the image.5- The system of high-speed cameras operating in the proposed optical system. It works in a microsecond synchronization system. This is a very suitable time, as images are taken from each camera separately and the 3D composition of the final image is synchronized with a delay time of 15 microseconds.

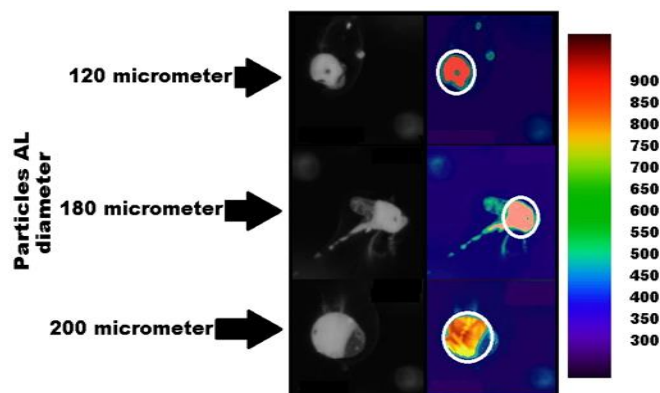


Fig.53. aluminum particles in a solid rocket fuel exhaust flame.

## 5. CONCLUSION

The proposed optical system in evaluating solid rocket fuel combustion performance is one of the methods based on accurate analysis and safety performance. The proposed optical system succeeded in conducting comprehensive spectral analysis of solid rocket fuel combustion products at a distance. Through a promising design of optical systems, each part has been explained in detail, and the design steps and the final shape of the manufactured product have been taken into consideration step by step. Images captured by the system using spectroscopy show an accurate analysis of the combustion products. The system also eliminates the shortcomings of individual spectral analysis systems. Since the system relies mainly on visual sub-systems that work in harmony with each other to achieve the desired goal. Whereas, the laser imaging technique was used to pass the laser beams towards the combustion products to illuminate the burning particles of fuel such as aluminum and receive them on the fast cameras by means of a light divider and draw a precise shape for the combustion products. A thermal camera was used with a promising optical system that was designed and implemented to protect the thermal camera and provide high-resolution images of fuel combustion products.

## 6. References

- Ross M. , Danilin M, Weisenstein D, A Ko, M. K. W, **2004** Ozone depletion caused by NO and H<sub>2</sub>O emissions from hydrazine-fueled rockets, *Journal of Geophysical Research: Atmospheres*, 109, 148-227, <https://doi.org/10.1029/2003JD004370> .
- Beier, Kurt, Lindermeir and Erwin, **2007** Comparison of line-by-line and molecular band IR modeling of high-altitude missile plume, *journal jqsrt*, 105, 111-127, <https://ui.adsabs.harvard.edu/abs/2007JQSRT.105..111B>.
- Toscano A, Lato M, Fontana D, De G and M.G. **2022** Optical Diagnostics for Solid Rocket Plumes Characterization: A Review. *Energies*, 15, 1470. <https://doi.org/10.3390/en15041470>.
- Merrill W, Beck S, Karthik P, and Piyush T, Vigor Y, **2007** Modeling of combustion and ignition of solid-propellant ingredients, *Progress in Energy and Combustion Science*, volume 33, Issue 6, Page 497-551, <https://doi.org/10.1016/j.pecs.2007.02.003>.
- De Luca, L.T., Galfetti, L., Severini, F. et al. **2005**, Burning of Nano-Aluminized Composite Rocket Propellants. *Combust Explos Shock Waves*, 41, 680–692. <https://doi.org/10.1007/s10573-005-0080-5>.
- Galfetti L, De L, F S, Meda L and G. M, M Marc and M Regi, S. Bellucc. **2006** Nanoparticles for solid rocket propulsion, *Journal of Physics: Condensed Matter*, 18, 19-91, <https://dx.doi.org/10.1088/0953-8984/18/33/S15>.
- Djalal T, Filippo M, Ilaria P, Luigi T, DeLuca, Kamel K, Marco F , Stefano D and Giov C. **2019** Effect of amide-based compounds on the combustion characteristics of composite solid rocket propellants, *Arabian Journal of Chemistry*, 12(8),3639-3651, <https://doi.org/10.1016/j.arabjc.2015.11.016>.
- De. L, Shimada T., Sinditskii V., Calabro M, Eds, **2016**, *Chemical rocket propulsion: A comprehensive survey of energetic materials*, Springer: Berlin/Heidelberg, Germany. 191–234, <https://link.springer.com/content/pdf/10.1007/978-3-319-27748-6>.
- Li Z, Wang, Ningfei, Shi, Baolu, Li, Shipeng, and Yang R, **2019** Effects of particle size on two-phase flow loss in aluminized solid rocket motors, *journal Acta Astronautical*, 159, 33-40, <https://ui.adsabs.harvard.edu/abs/2019AcAau.159...33L> .
- Ko J, Lee E and Kwon, S. **2019**, Influence of optical properties of alumina particles on the radiative base heating from solid rocket plume. *Adv. Space Res*, 64, 514–526. <https://doi.org/10.1016/j.asr.2019.04.024>.
- Kuzmin V, Marat kE, and Ruk.A, RV, **2015**, thermal radiation of heterogeneous combustion products in the model rocket engine plume, *journal The rmophysics and Aeromechanics*, 22, 371-386, <https://doi.org/10.1134/S0869864315030129>.
- Parry, D.L and Brewster, Q.M. **2012**. Optical constants of Al<sub>2</sub>O<sub>3</sub> smoke in propellant flames. *Journal of thermophysics and heat transfer*, 5, 142–149, <https://doi.org/10.2514/3.241>.
- Giechaskiel, Barouch, Clairotte and M, M, **2021**, Fourier Transform Infrared (FTIR) Spectroscopy for Measurements of Vehicle Exhaust Emissions: A Review, *journal Applied Sciences*, volume 11, pages 16-74, <https://doi.org/10.3390/app11167416>.
- Gill, Walter Cruz.C, Alvaro A , Donaldson A , Lim.J , Sivathanu, Y , Bystrom, E , Haug A , Sharp, L and Surmick D, **2014**, Combustion diagnosis for analysis of solid propellant rocket abort hazards: Role of spectroscopy, *Journal of Physics: Conference Series*, 548, 70 -90, <https://dx.doi.org/10.1088/1742-6596/548/1/012055>.
- Bakhir L, Levashenko G. and Tamanovich, **1977**. Refinement of the imaginary part of the complex refractive index of liquid aluminum oxide. *J Appl Spectrosc* , 26, 378–383 . <https://doi.org/10.1007/BF00617449>.
- Van H, H C, **1957** *Light Scattering by Small Particles* John Wiley & Sons, journal Inc. New York, volume 470, 134:157 <https://doi.org/10.1002/qj.49708436025>.
- Bitjukov, Vladimir K and Petrov V, **2013** , Absorption coefficient of molten aluminum oxide in semitransparent spectral range, *journal Applied Physics Research*, 5, 51:60, : <http://dx.doi.org/10.5539/apr.v5n1p51>.
- Jackson T Najjar F and Buckmaster J. **2005** New aluminum agglomeration models and their use in solid propellant-rocket simulations. *Journal of Propulsion and Power*, 21, 925–936, <https://doi.org/10.2514/1.11888>.
- Lengell'e, G , Duterque J and Trubert J. **2002** Combustion of solid propellants. In *RTO/VKI Special Course on Internal Aerodynamics in Solid Rocket Propulsion* held in Rhode-Saint-Genève, Belgium 78 , 1–62, published in RTO-EN-023-4. <https://apps.dtic.mil/sti/pdfs/ADA425264.pdf>.
- Karasev V, Onischuk A, Glotov O Baklanov A, Maryasov A, Zarko V , Panfilov V, Levykin A, and Sabelfeld K. **2004** Formation of charged aggregates of Al<sub>2</sub>O<sub>3</sub> nanoparticles by combustion of aluminum droplets in air. *Combust. Flame*, volume 138, page 40–54. <https://doi.org/10.1016/j.combustflame.2004.04.001>.
- Reed R and Calia, **1993** Review of aluminum oxide rocket exhaust particles., 28th Thermophysics Conference. <https://doi.org/10.2514/6.1993-2819>.
- Epikhin V, Vizen F, and Magomedov Z. et al. **2018** Polarizer-Free Acousto-Optic Monochromators. *Tech. Phys.* 63, 1040–1043, <https://doi.org/10.1134/S1063784218070113>.

23. L. Li A , Mostovshchikov A , Ilyin A , Smirnov and F. A, **2020** "Optical System With Brightness Amplification for Monitoring the Combustion of Aluminum-Based Nanopowders," in IEEE Transactions on Instrumentation and Measurement, 69 (2),457-468, <https://ieeexplore.ieee.org/document/8680023>.
24. Sandra G, Masoumeh K , Jenny A , Anders B , Maria S , Thomas S Annelie F, and Malin L, **2018** Mass spectrometry profiling reveals altered plasma levels of monohydroxy fatty acids and related lipids in healthy humans after controlled exposure to biodiesel exhaust, journal Analytica Chemical Acta , 1018 , 62-69 , <https://doi.org/10.1016/j.aca.2018.02.032>.
25. Oscano A, Lato M , Fontanarosa, D De G, and M.G. **2022** Optical Diagnostics for Solid Rocket Plumes Characterization: A Review. Energies, 15, 14-70. <https://doi.org/10.3390/en15041470>.
26. Hashim S, Srinibas K, Arnab R, and Suneel K . **2018** "Regression rates and burning characteristics of boron-loaded paraffin-wax solid fuels in ducted rocket applications." *Journal Combustion and Flame*, 191, 287-297 <https://doi.org/10.1016/j.combustflame.2018.01.018>.
27. Feng, Yunchao, Likun M, Zhixun X Liya H , and Dali Y. **2020** "Ignition and combustion characteristics of single gas-atomized Al-Mg alloy particles in oxidizing gas flow." journal Energy , 196, 110-36, <https://doi.org/10.1016/j.energy.2020.117036>.
28. Tian, Hui, Zhongshuo W, Zihao G, Ruipeng Y, Guobiao C, and Yuanjun Z. **2022** "Effect of metal and metalloid solid-fuel additives on performance and nozzle ablation in a hydroxy-terminated polybutadiene-based hybrid rocket motor." journal Aerospace Science and Technology 123, 107-193, <https://doi.org/10.1016/j.energy.2020.117036>.
29. Gu J, Wei W, and Dan Y. **2021** "Temperature control and low infrared emissivity double-shell phase change microcapsules and their application in infrared stealth fabric." *Progress in Organic Coatings*, 159, 106-439 <https://doi.org/10.1016/j.porgcoat.2021.106439>.
30. Wang F, Junyan L, Peng S, Jinlong G, Wei P, Guobin L, and Mingjun C, **2022** "Multimodal optical excitation pulsed thermography: Enhanced recognize debonding defects of the solid propellant rocket motor cladding layer." *Mechanical Systems and Signal Processing* 163, 108-164 <https://doi.org/10.1016/j.ymsp.2021.108164>.
31. Yilmaz, Nadir, Francisco V, Jonathan H, Burl D, and Walt G. "Rocket motor exhaust thermal environment. Characterization." *Journal Measurement* 122 , 312-319, <https://doi.org/10.1016/j.measurement.2018.03.039> .
32. Li, Guoshuai, Muhammed B Agir, Konstantinos K, Takahiro U, and Sriram R. **2019** "Image processing techniques for shock wave detection and tracking in high speed schlieren and shadowgraph systems." In *Journal of Physics: Conference Series*, 1215, 12-21. <https://dx.doi.org/10.1088/1742-6596/1215/1/012021>.
33. Luthman, Elizabeth, Niccolo C, Daniel L, Graham C, and Paul D. **2019** "Simulating schlieren and shadowgraph images from LES data." *Journal Experiments in Fluids* , 60, 1-16 , <https://doi.org/10.1007/s00348-019-2774-6>.
34. . Znamenskaya, Irina A, Igor A , and Doroshchenko. **2021** "Edge detection and machine learning for automatic flow structures detection and tracking on schlieren and shadowgraph images." *Journal of Flow Visualization and Image Processing* 28(4) [https://www.dl.begellhouse.com/journals/52b74bd3689ab10b\\_08ce4b7653aa2ba3\\_403eb2791b29c77b.html](https://www.dl.begellhouse.com/journals/52b74bd3689ab10b_08ce4b7653aa2ba3_403eb2791b29c77b.html).
35. Smith, Cary D, Mark T, Gragston, Zhili Z, Timothy O, Campbell D , Carter X , Louis J, Santodonato, and Hassina Z. **2019** "Simultaneous Neutron Radiography of Metal Nozzle Geometry and Near-Field Spray." *Journal of Propulsion and Power*, 35,419-423 <https://doi.org/10.2514/1.B37304>.
36. Settles and Gary S. **2018** "Smartphone schlieren and shadowgraph imaging." *Journal Optics and Lasers in Engineering* 104, 9-21, <https://doi.org/10.1016/j.optlaseng.2017.07.002>.
37. Aphale, Siddhant, Gabriel S, Paul D. **2020** "Development of a non-intrusive flame to fuel surface radiative heat flux measurement for hybrid rockets." *Journal In AIAA Propulsion and Energy Forum*, 16, 37-48 , <https://doi.org/10.2514/6.2020-3748> .

38. Geipel, Clayton M, Christopher J. Pfützner, and Brian T. **2022** "Active Control of Fuel Position in Opposed-Flow Strand Burner Experiments." *Journal Combustion Science and Technology*, **20** 1-18. <https://doi.org/10.1080/00102202.2022.2114796>.
39. Merzkirch W. **1987** *Techniques of Flow Visualization*; north Atlantic treaty organization—Advisory Group for Aerospace Research and Development; Institute für Thermo und Fluidodynamik Ruhr-Universität Bochum: Bochum, Germany; Gradiographs **45**, 302. <https://apps.dtic.mil/sti/citations/ADA194291>.
40. Hargather M , and Settles G. **2010** Recent Developments in Schlieren and Shadowgraph. In Proceedings of the 27th AIAA Aerodynamic Measurement Technology and Ground Testing, Chicago, IL, USA, <https://doi.org/10.2514/6.2010-4206>.
41. Krehl P , Engemann S. August T,**1995** The first who visualized shock waves. *Journal Shock Waves* **5**, 1–18 <https://doi.org/10.1007/BF02425031>.
42. Nakaya, Shinji, Hajime Yamana, and Mitsuhiro Tsue. **2021** "Experimental investigation of ethylene/air combustion instability in a model scramjet combustor using image-based methods." *Journal Proceedings of the Combustion Institute* , volume **38**, page 3869-3880, <https://doi.org/10.1016/j.proci.2020.07.129>.
43. Chen, Yi, Daniel R. Guildenbecher, Kathryn N, Marcia A. Cooper L, Oliver, and Ephraim B. **2017** "Study of aluminum particle combustion in solid propellant plumes using digital in-line holography and imaging pyrometry." *Combustion and Flame* **182**,225-237. <https://doi.org/10.1016/j.combustflame.2017.04.016>.
44. Chen, Yi, Jeffery D. Heyborne, and Daniel R. **2018** "Time-resolved digital in-line holography and pyrometry for aluminized solid rocket propellants." In *Laser Applications to Chemical, Security and Environmental Analysis*. Optical Society of America, <https://opg.optica.org/abstract.cfm?URI=LACSEA-2018-LTu3C.5>.
45. Guildenbecher, Daniel R, Marcia A, Walter G, Howard L, Michael S. Oliver, Thomas W and Grasser.**2014** "Quantitative, three-dimensional imaging of aluminum drop combustion in solid propellant plumes via digital in-line holography.2019" *Optics* **39**(17) 5126-5129. <https://opg.optica.org/ol/abstract.cfm?URI=ol-39-17-5126>.
46. Mirzaeian H , Manjooran S, and Major A, **2014**,A simple technique for accurate characterization of thermal lens in solid state lasers, *journal , Photonics North* ,**9**288, 35-43 <https://doi.org/10.1117/12.2075117>.
47. Iffländer R . 2001. *Solid-state lasers for materials processing: fundamental relations and technical realizations* (Vol. 77). Springer Science <https://link.springer.com/search?query=&search-within=Journal&facet-journal-id=42452>.
48. Peyre C , Fumery, and Gatinel D.**2005** "Comparison of high-order optical aberrations induced by different multifocal contact lens geometries." *Journal francais ophthalmology* **28**, 599-604, [https://doi.org/10.1016/s0181-5512\(05\)81101-5](https://doi.org/10.1016/s0181-5512(05)81101-5).
49. Yoder P, nad Vukobratovich, D., **2017** *Opto-Mechanical Systems Design, Volume 2: Design and Analysis of Large Mirrors and Structures, Vol. 2*. Crc Press. <https://doi.org/10.1201/b18136>.
50. Paul R and Yoder J, **1981**"Optomechanical Systems Design," *journal Optical Engineering* volume **20**,page 155-222 <https://doi.org/10.1117/12.7972682>.
51. Xiao,Gand L ,An S and Xiaoxue Y, **2013** Tunable slow light in a quadratically coupled optomechanical system, *Journal of Physics B: Atomic, Molecular and Optical Physics*, **46**, 025501, <https://dx.doi.org/10.1088/0953-4075/46/2/025501>.
52. Xu, Xun W , Li Y. **2015**, Optical nonreciprocity and optomechanical circulator in three-mode optomechanical systems, *journal Phys. Rev. A* , **91** ,53 -85, <https://link.aps.org/doi/10.1103/PhysRevA.91.053854>.
53. He Q, Zhao Z, Ye X, Luo C, Zhang D, Wang S, Xu X. **2022** Optical Coupling Efficiency of a Coupler with Double-Combined Collimating Lenses and Thermally Expanded Core Fibers. *Micromachines.*; **13**(2):324. <https://doi.org/10.3390/mi13020324>.
54. Gade, R., Moeslund, T.B. **2014** Thermal cameras and applications: a survey. *Machine Vision and Applications* **25**, 245–262 <https://doi.org/10.1007/s00138-013-0570-5>.
55. Mariusz F, Mariusz R. Rychter, and Bogusław W. (2022) Non-destructive testing of metal archaeological relics on the example of zinc dog tags discovered during the exhumation of people murdered in the Remand Prison at 37 Rakowiecka Street in Warsaw. *Journal of Cultural Heritage* **57**, 149-153. <https://doi.org/10.1080/17686733.2021.1962096>.
56. Niu, Qinglin, Peng G, Zhichao Y, Zhihong H, and Shikui D.**2019** "Numerical analysis of thermal radiation noise of shock layer over an infrared optical dome at near-ground altitudes." *Journal Infrared Physics & Technology*, **97**, 74-84., <https://doi.org/10.1016/j.infrared.2018.12.020>.
57. Karar, V, and Amit L.**2021** "Design and fabrication of multilayer dichroic beam splitter." *Journal Advanced Materials Proceedings* **2**, (6)398-401, [https://amp.iaamonline.org/article\\_16308.html](https://amp.iaamonline.org/article_16308.html).
58. Xing Z., Hong Y and Zhang B. **2018** The influence of dichroic beam splitter on the airborne multiband co-aperture optical system. *Optoelectronic. Lett.* **14**, 252–256 . <https://doi.org/10.1007/s11801-018-7273-0>.